2025, **26** (3), 380–395. doi 10.26089/NumMet.v26r325

doi 10.26089/NumMet.v26r325

Application of the nudging technique to produce initial states for the INM RAS climate model seasonal hindcasts

Maria A. Tarasevich
Marchuk Institute of Numerical Mathematics RAS, Moscow, Russia
Hydrometeorological Research Center of Russian Federation, Moscow, Russia
ORCID: 0009-0002-1353-2711, e-mail: mashatarasevich@gmail.com

Evgeny M. Volodin
Marchuk Institute of Numerical Mathematics RAS, Moscow, Russia
Institute of Geography RAS, Moscow, Russia
ORCID: 0000-0003-1073-7287, e-mail: volodinev@gmail.com

Abstract: This study examines the implementation of nudging in the INM RAS global coupled climate model to improve the initial states for seasonal hindcasts. We compare results of three nudging experiments with both reanalyses data and ensemble of CMIP6 historical experiments. The results show that nudging significantly reduces model biases in atmosphere and ocean fields. The experiment with nudging excluding lower atmospheric levels yields the best performance by minimizing the impact of the relaxation procedures on the model physics in the atmosphere boundary layer. We compare the quality of the hindcasts for November–March obtained with different initialization techniques. The initialization approach using nudging outperforms other initialization methods for hindcasts of the Northern Hemisphere winter season with one-month lead time. However, for the first forecast month the full field initialization demonstrates the best results. The study highlights that nudging in the ocean model is essential to maintain hindcast skill over longer lead times and proposes nudging as a promising approach for initialization of the annual-to-decadal climate predictions.

Keywords: INM RAS climate model, nudging, seasonal hindcasts, initialization.

Acknowledgements: This research was carried out at the Marchuk Institute of Numerical Mathematics of the Russian Academy of Sciences and supported by the Russian Science Foundation, project 25–17–00203, in Sections 3, 4 and by the Moscow Center of Fundamental and Applied Mathematics at INM RAS (Agreement with the Ministry of Education and Science of the Russian Federation № 075–15–2025–347) in Section 6. All computations were performed using the HPC system of the Marchuk Institute of Numerical Mathematics of the Russian Academy of Sciences and the Cray XC40-LC HPC system at the MCC of Roshydromet.

For citation: M. A. Tarasevich, E. M. Volodin, “Application of the nudging technique to produce initial states for the INM RAS climate model seasonal hindcasts”, Numerical Methods and Programming. **26** (3), 380–395 (2025). doi 10.26089/NumMet.v26r325.

2025, **26** (3), 380–395. doi 10.26089/NumMet.v26r325

Применение метода подталкивания с целью получения начальных состояний для сезонных ретроспективных прогнозов климатической модели ИВМ РАН

М. А. Тарасевич
Институт вычислительной математики РАН имени Г. И. Марчука,
Москва, Российская Федерация
Гидрометеорологический научно-исследовательский центр Российской Федерации,
Москва, Российская Федерация
ORCID: 0009-0002-1353-2711, e-mail: mashatarasevich@gmail.com

Е. М. Володин
Институт вычислительной математики РАН имени Г. И. Марчука,
Москва, Российская Федерация
Институт географии РАН, Москва, Российская Федерация
ORCID: 0000-0003-1073-7287, e-mail: volodinev@gmail.com

Аннотация: В данном исследовании рассматривается применение метода подталкивания в глобальной климатической модели ИВМ РАН для улучшения начальных состояний для сезонных ретроспективных прогнозов. Результаты трех климатических экспериментов с подталкиванием сравниваются с данными реанализов и ансамблем исторических экспериментов по протоколу CMIP6. Применение метода подталкивания позволяет значительно уменьшить ошибки модели в воспроизведении атмосферных и океанических полей. Эксперимент, в котором подталкивание не применяется к приземным атмосферным уровням, показывает наилучшие результаты за счет уменьшения влияния процедур подталкивания на физику пограничного слоя модели атмосферы. Проводится сравнение качества ретроспективных прогнозов на ноябрь–март, полученных с использованием различных методов инициализации. Подход с использованием начальных состояний по данным расчетов с подталкиванием превосходит другие методы инициализации для ретроспективных прогнозов на зимний сезон Северного полушария с заблаговременностью один месяц. Однако для первого месяца прогноза наилучшие результаты демонстрирует инициализация полными полями. В работе подчеркивается необходимость использования подталкивания в модели океана для обеспечения качественного прогноза с большой заблаговременностью, а также предлагается применение этого метода для инициализации климатических прогнозов на год–десятилетие.

Ключевые слова: климатическая модель ИВМ РАН, метод подталкивания, ретроспективные сезонные прогнозы, инициализация.

Благодарности: Работа выполнена в Институте вычислительной математики имени Г. И. Марчука Российской академии наук при поддержке Российского научного фонда (грант 25–17–00203), разделы 3 и 4, и Отделения Московского центра фундаментальной и прикладной математики в ИВМ РАН (Соглашение с Минобрнауки России № 075–15–2025–347), раздел 6. Все расчеты выполнены с использованием вычислительной системы Института вычислительной математики имени Г. И. Марчука Российской академии наук и вычислительной системы Cray XC40-LC ГВЦ Росгидромета.

Для цитирования: Тарасевич М.А., Володин Е.М. Применение метода подталкивания с целью получения начальных состояний для сезонных ретроспективных прогнозов климатической модели ИВМ РАН // Вычислительные методы и программирование. 2025. **26**, № 3. 380–395. doi 10.26089/NumMet.v26r325.

2025, **26** (3), 380–395. doi 10.26089/NumMet.v26r325

1. Introduction. The INM RAS climate model (INMCM) is a coupled general circulation model. The INMCM5 [1] version of the INM RAS climate model participated in the Coupled Model Intercomparison Project Phase 6 (CMIP6) [2]. The INMCM5 is able to simulate both the present-day climate [1, 3, 4], and its changes [5]. The results of the climate change projections for various scenarios [6, 7] are also in good agreement with the ones obtained using other CMIP6 climate models [8].

Following the seamless approach [9–11] the systems of seasonal [12, 13] and annual-to-decadal [14] forecast based on the INMCM5 system were developed. Both the seasonal [15–17] and annual-to-decadal [14, 18] prediction systems demonstrate good predictability of the large-scale modes of climate variability and the Arctic sea ice state. The INMCM5 seasonal forecast system was run operationally at the Hydrometcenter of Russia from November 2023 to December 2024. The annual-to-decadal forecast system based on INMCM5 is run operationally at the Hydrometcenter of Russia from November 2023.

Further enhancement of seasonal and annual-to-decadal prediction systems based on the INM RAS climate model may be related to physical model improvements and development of the initialization techniques. Since the initial data significantly affects the forecast on the seasonal timescale, in this study we focus on the INMCM5 seasonal prediction system initialization. There is no common recommendation on which initialization method provides the best seasonal forecast quality, so for each prediction system it is an important research question to be answered [19, 20]. The development of the INMCM5 seasonal prediction system started with the anomaly initialization technique [21], later the full field initialization approach [22] was implemented using the data from reanalyses ERA5 [23] and SODA3.4.2 [24, 25]. The common problem of the INMCM5 initialization with anomaly and full field techniques is that the initial conditions are created using reanalyses data produced by other models. This may lead to initialization shocks [26], which affect the quality of seasonal predictions. Gradually making the initialization of the INM RAS climate model seasonal prediction system more sophisticated, in this paper we implement the nudging (or Newtonian relaxation) technique [27] to produce initial states for atmosphere, land surface and ocean that are consistent with both observational data and model physics and dynamics. Nudging is widely used in atmosphere and ocean components of the various decadal prediction systems [28–30]. For seasonal forecast systems, more complicated data assimilation methods (3D-Var, 4D-Var, Ensemble Kalman filter [31]) are commonly used [32, 33] to produce initial states for each component separately, while NorCPM [19] and CanSIPS [34] utilize nudging in weakly coupled assimilation systems [35].

We also analyze the climate simulated by INMCM5 with nudging and then use the initial states from these experiments to start series of hindcasts for November–March period. The Northern Hemisphere winter hindcasts are of particular interest due to strong stratosphere impact on the troposphere dynamics [36, 37] and the greatest remote response of mid-latitudes to the El Niño–Southern Oscillation phenomenon [38, 39]. We compare the quality of the obtained hindcasts with those initialized using anomaly and full field initialization techniques. The goal of this paper is to demonstrate that the proposed relaxation technique for producing initial states improves the skill of the seasonal hindcasts without requiring large amount of additional computational resources.

The paper is organized as follows. In Section 2 of the paper a description of the INM RAS climate model used in this study is given. Sections 3 and 4 describe an implementation of nudging in the INMCM5 and the results of the climate simulation with the relaxation applied. Section 5 introduces description of the INMCM5 seasonal hindcast technology. Section 6 presents the results of seasonal hindcasts obtained using initial states from different relaxation experiments. In Section 7 the conclusion and discussion of the obtained results are outlined.

2. The INMCM5 climate model. The INMCM5 global coupled climate model [1] consists of the atmosphere model with an aerosol [40] and land surface [41] modules, and the ocean model [42] with the module of sea ice dynamics with elastic-viscous-plastic rheology and thermodynamics with single thickness gradation [43]. The interactive aerosol module describes the evolution of the concentration of 10 substances. The spatial resolution of the atmosphere model is $2^\circ \times 1.5^\circ$ and 73 vertical σ-levels up to $\sigma = 0.0002$ (about 60 km). The vertical step in the lower and middle stratosphere is close to 500 m, whereas below and above its value increases to 1000–1500 m. The time step in the atmosphere dynamic core is 3 minutes for this spatial resolution. The ocean model has a horizontal resolution of $0.5^\circ \times 0.25^\circ$ and 40 vertical σ-levels. The time step in the ocean model is 12 minutes.

2025, **26** (3), 380–395. doi 10.26089/NumMet.v26r325

The atmosphere model is based on the following system of equations in the hydrostatic approximation [44]:

$$\frac{du}{dt} - \left(f + \frac{u}{a}\tan\varphi\right)v + \frac{1}{a\cos\varphi}\left(\frac{\partial\Phi}{\partial\lambda} + \frac{RT}{p_s}\frac{\partial p_s}{\partial\lambda}\right) = F_u, \tag{1}$$

$$\frac{dv}{dt} + \left(f + \frac{u}{a}\tan\varphi\right)u + \frac{1}{a}\left(\frac{\partial\Phi}{\partial\varphi} + \frac{RT}{p_s}\frac{\partial p_s}{\partial\varphi}\right) = F_v, \tag{2}$$

$$\frac{\partial\Phi}{\partial\sigma} = -\frac{RT}{\sigma}, \tag{3}$$

$$\frac{dT}{dt} - \frac{RT}{p_s C_p}\left(\frac{\partial p_s}{\partial t} + \frac{u}{a\cos\varphi}\frac{\partial p_s}{\partial\lambda} + \frac{v}{a}\frac{\partial p_s}{\partial\varphi} + \frac{p_s\dot\sigma}{\sigma}\right) = F_T + \varepsilon, \tag{4}$$

$$\frac{dq}{dt} = F_q - (C - E), \tag{5}$$

$$\frac{\partial p_s}{\partial t} + \frac{1}{a\cos\varphi}\left(\frac{\partial p_s u}{\partial\lambda} + \frac{\partial p_s v\cos\varphi}{\partial\varphi}\right) + \frac{\partial p_s\dot\sigma}{\partial\sigma} = 0. \tag{6}$$

Here λ is the longitude [rad], φ is the latitude [rad], a is the Earth's radius [m], $\sigma = p/p_s$ is the vertical coordinate, p is the air pressure [Pa], p_s is the surface air pressure [Pa], t is the time [s], T is the absolute temperature [K], u, v are zonal and meridional velocity components respectively [m/s], $\dot\sigma$ is vertical velocity component [1/s], q is the specific humidity, f is the Coriolis parameter [rad/s], Φ is the geopotential [m^2/s^2], R is the specific air gas constant [J/(kg · K)], C_p is the air heat capacity at constant pressure [J/(kg · K)], F_u, F_v, F_T, F_q are the physical tendencies of momentum, temperature and humidity correspondingly, ε is the radiative heating tendency, C and E describes the moisture condensation and evaporation, $\dfrac{d}{dt}$ is the total time derivative.

The ocean model solves a set of the large-scale hydrothermodynamic equations in hydrostatic and Boussinesq approximations:

$$D_t u_\mathrm{o} - (f+\chi)v_\mathrm{o}H = -\frac{H}{r_x}\left(\frac{1}{\rho_0}\frac{\partial(P+p_a)}{\partial x} - g\frac{\partial\zeta}{\partial x}\right) + \frac{\partial}{\partial\sigma_\mathrm{o}}\left(\frac{\nu}{H}\frac{\partial u_\mathrm{o}}{\partial\sigma_\mathrm{o}}\right) + \mathcal{F}u_\mathrm{o}, \tag{7}$$

$$D_t v_\mathrm{o} + (f+\chi)u_\mathrm{o}H = -\frac{H}{r_y}\left(\frac{1}{\rho_0}\frac{\partial(P+p_a)}{\partial y} - g\frac{\partial\zeta}{\partial y}\right) + \frac{\partial}{\partial\sigma_\mathrm{o}}\left(\frac{\nu}{H}\frac{\partial v_\mathrm{o}}{\partial\sigma_\mathrm{o}}\right) + \mathcal{F}v_\mathrm{o}, \tag{8}$$

$$\frac{\partial\zeta}{\partial t} = \frac{1}{r_x r_y}\left(\frac{\partial}{\partial x}(r_y u_\mathrm{o}H) + \frac{\partial}{\partial y}(r_x v_\mathrm{o}H)\right) + \frac{\partial w_\mathrm{o}}{\partial\sigma_\mathrm{o}}, \tag{9}$$

$$\widetilde{D_t}\theta = \frac{\partial}{\partial\sigma_\mathrm{o}}\left(\frac{\nu_\theta}{H}\frac{\partial\theta}{\partial\sigma_\mathrm{o}}\right) + \mathcal{D}\theta + F_\theta, \tag{10}$$

$$\widetilde{D_t}S = \frac{\partial}{\partial\sigma_\mathrm{o}}\left(\frac{\nu_S}{H}\frac{\partial S}{\partial\sigma_\mathrm{o}}\right) + \mathcal{D}S + F_S, \tag{11}$$

$$\rho = \hat\rho(\theta, S, P). \tag{12}$$

Here x and y are the generalized orthogonal coordinates on a rotated sphere [dimensionless], z is the depth coordinate [m], r_x and r_y are the metric coefficients [m], H is the ocean depth at rest [m], ζ is the deviation of the free surface level [m], $h = H - \zeta$ is the effective depth [m], the vertical coordinate σ_o is given by $\sigma_\mathrm{o} = \dfrac{z-\zeta}{H-\zeta}$, u_o, v_o and w_o are the components of the flow velocity [m/s], $\chi = \dfrac{1}{r_x r_y}\left(v_\mathrm{o}\dfrac{\partial r_y}{\partial x} - u_\mathrm{o}\dfrac{\partial r_x}{\partial y}\right)$, P is the hydrostatic pressure of the water column [Pa], p_a is the atmospheric pressure at sea surface level [Pa], θ is the sea water potential temperature [°C], S is the sea water salinity [PSU, practical salinity unit], ρ is the water density [kg/m^3] governed by equation of state (12), $\rho_0 = 1025$ kg/m^3 is the background density, ν, ν_θ and ν_S are the coefficients of vertical turbulent viscosity and diffusion respectively [m^2/s], g is the free fall acceleration [m/s^2].

Operators

$$D_t\psi = \frac{1}{2}\left[h\frac{\partial\psi}{\partial t} + \frac{\partial(h\psi)}{\partial t}\right] + \frac{1}{2r_x r_y}\left[r_y H u_\mathrm{o}\frac{\partial\psi}{\partial x} + \frac{\partial}{\partial x}(r_y H u_\mathrm{o}\psi) + r_x H v_\mathrm{o}\frac{\partial\psi}{\partial y} + \frac{\partial}{\partial y}(r_x H v_\mathrm{o}\psi)\right] + \frac{1}{2}\left[w_\mathrm{o}\frac{\partial\psi}{\partial\sigma_\mathrm{o}} + \frac{\partial(w_\mathrm{o}\psi)}{\partial\sigma_\mathrm{o}}\right]$$

2025, **26** (3), 380–395. doi 10.26089/NumMet.v26r325

and

$$\widetilde{D_t}\psi = \frac{\partial(h\psi)}{\partial t} + \frac{1}{r_x r_y}\left[\frac{\partial}{\partial x}\left(r_y H u_\mathrm{o}\psi\right) + \frac{\partial}{\partial y}\left(r_x H v_\mathrm{o}\psi\right)\right] + \frac{\partial(w_\mathrm{o}\psi)}{\partial\sigma_\mathrm{o}}$$

describe advection in a semi-conservative and conservative form, $\mathcal{F} = -\kappa\Delta^4$ describes 8^{th}-order horizontal viscosity for velocities with diffusion coefficient κ [m^8/s] and $\mathcal{D}$ describes isopycnic diffusion for tracers, quantities F_θ and F_S stand for physical tendencies for temperature and salinity, including penetrative solar radiance and fresh water flux.

3. Implementation of nudging. An additional term in form $\dfrac{X_R - X}{\tau}$ is added to the right hand side of the prognostic equation for some variable X. This term can be viewed as nudging of the variable X to its observed value X_R with characteristic time τ. In other words, variable X is nudged to value X_R. The parameter τ controls the strength of the relaxation. Large values of τ produce mild corrections of X towards X_R but may not be sufficient to bring the model trajectory to the observed one. In contrast, small values of τ couple X and X_R tightly, but may break relations between X and other model variables.

Nudging allows to obtain a self-consistent state of the model variables. For example, nudging of the atmospheric state enables to get a consistent state of such land surface variables as snow water equivalent, soil temperature and moisture.

In this work, we use reanalyses data as observations because it is a natural source of gridded global data and do not require additional preprocessing and quality control procedures.

3.1. The atmosphere model. For the INMCM5 atmosphere model we choose to perform relaxation for the wind velocities and temperature only. The corresponding physical tendencies for the equations (1), (2) and (4) were replaced with

$$\widetilde{F_u} = F_u + \frac{u_R - u}{\tau_\mathrm{atm}},$$
$$\widetilde{F_v} = F_v + \frac{v_R - v}{\tau_\mathrm{atm}},$$
$$\widetilde{F_T} = F_T + \frac{T_R - T}{\tau_\mathrm{atm}}.$$

Nudging tendencies are computed and explicitly added to the prognostic variables at each dynamical step. The values of u_R, v_R and T_R are obtained from the ERA5 [23] reanalysis on the 37 pressure levels. Reanalysis data has 3 hour temporal resolution and is interpolated linearly for the current simulation time. Data is also linearly interpolated along the vertical coordinate to the model pressure levels at $p_k = p_s\sigma_k$.

Let us consider the numerical scheme of nudging for the atmosphere model in details. The INMCM5 atmosphere model uses the symmetric second-order finite-difference approximations for spatial operators in the system (1)–(6). The temporal discretization employs a splitting technique [45] to separately integrate different physical processes. Tendencies computed by physical parameterizations, including the nudging term, are integrated independently of the dynamical core. The core itself integrates the dynamics equations using the leap-frog scheme with semi-implicit treatment for fast processes.

The simplified numerical scheme [44] of the atmosphere model (1)–(6) can be written as

$$\frac{\tilde{X}^n - X^n}{2\Delta t} = F(X^n), \tag{13}$$

$$\frac{X^{n+1} - \tilde{X}^{n-1}}{2\Delta t} = A_\mathrm{e}(\tilde{X}^n) + A_\mathrm{si}\frac{X^{n+1} + \tilde{X}^{n-1}}{2}. \tag{14}$$

Here X is the state vector, $F(X)$ stands for the physical tendencies. The dynamical tendencies are made up of the explicit part $A_\mathrm{e}(X)$ and the linear semi-implicit part $A_\mathrm{si}X$. The latter consists of the terms responsible for propagation of the gravitational waves. Semi-implicit approach relaxes the Courant's restriction on the time step Δt by a factor of 4–5. For the sake of simplicity the spatial near-pole filtration and temporal Asselin filtration are omitted from the scheme.

To analyze the stability properties of the scheme, we consider auxiliary scalar model equation $\dot{x} = i\omega x$, reflecting the skew-symmetrical nature of the dynamics operator. For the model equation the scheme (13), (14)

2025, **26** (3), 380–395. doi 10.26089/NumMet.v26r325

results in

$$\frac{\tilde{x}^n - x^n}{2\Delta t} = \frac{x_R - x^n}{\tau_{\text{atm}}}, \tag{15}$$

$$\frac{x^{n+1} - \tilde{x}^{n-1}}{2\Delta t} = i\omega_L \tilde{x}^n + i\omega_H \frac{x^{n+1} + \tilde{x}^{n-1}}{2}. \tag{16}$$

In accordance with splitting $A = A_e + A_{si}$, the quantity ω is splitted into the slow low-frequency part ω_L and the fast high-frequency part ω_H.

Application of the von Neumann stability analysis to the scheme (15), (16) gives

$$\frac{\mu - 1}{2\Delta t} = -\frac{1}{\tau_{\text{atm}}},$$

$$\frac{\xi - \mu\xi^{-1}}{2\Delta t} = i\omega_L \mu + i\omega_H \frac{\xi + \mu\xi^{-1}}{2}.$$

Here $\mu = \tilde{\delta}^n/\delta^n$, $\xi = \delta^{n+1}/\delta^n$ and δ^n is the small perturbation of x^n. It immediately follows that $\mu = 1 - \dfrac{2\Delta t}{\tau_{\text{atm}}}$. We assume that $\mu > 0$, which is true when $\tau_{\text{atm}} > 2\Delta t$. The second equation reduces to a quadratic equation of the form $\xi^2(1 - i\omega_H\Delta t) - 2i\omega_L\Delta t\mu\xi - (1 + i\omega_H\Delta t)\mu = 0$. Its roots are given by

$$\xi_{1,2} = \frac{i\omega_L\Delta t\mu \pm \sqrt{D/4}}{1 - i\omega_H\Delta t}, \quad \frac{D}{4} = -(\omega_L\Delta t\mu)^2 + (1 - i\omega_H\Delta t)(1 + i\omega_H\Delta t)\mu = (1 + (\omega_H\Delta t)^2)\mu - (\omega_L\Delta t\mu)^2.$$

When $0 < \mu < 1$, the discriminant D is positive provided that $|\omega_L\Delta t| \leqslant 1$. If D is positive, then $|\xi_1| = |\xi_2|$. Moreover, $|\xi_1\xi_2| = \left|\dfrac{1 + i\omega_H\Delta t}{1 - i\omega_H\Delta t}\right| \mu = \mu < 1$.

The analysis shows that the scheme with nudging is stable provided that $|\omega_L\Delta t| \leqslant 1$ and $\tau_{\text{atm}} > 2\Delta t$. The first condition is the same that is required for the scheme stability without nudging. The second condition limits the stiffness of the nudging process and holds in practice.

The characteristic relaxation time τ_{atm} was chosen to be 6 hours. This value provides good agreement for the nudged fields u, v, T and their observed values u_R, v_R and T_R and satisfactory quality of simulation of other atmospheric fields.

Early attempts included q as a nudged variable, but nudging of q interfered with condensation processes in the model, leading to large errors in precipitation simulation.

3.2. The ocean model. For the ocean model, nudging is applied only for potential temperature θ and salinity S. The physical tendencies in the equations (10) and (11) were replaced by

$$\widetilde{F_\theta} = F_\theta + H\frac{\theta_R - \overline{\theta}^{1d}}{\tau_{\text{oc}}},$$

$$\widetilde{F_S} = F_S + H\frac{S_R - \overline{S}^{1d}}{\tau_{\text{oc}}}.$$

Like for the atmosphere model, the nudging tendencies are computed and added explicitly at each step. However, the reanalysis SODA3.4.2 [24, 25] provides only 5-day and monthly averaged data. Daily averaging removes diurnal cycle from the reanalysis data. This is the reason we replace X in relaxation tendency $\dfrac{X_R - X}{\tau}$ with its daily averaged value $\overline{X}^{1d}$ given by:

$$\overline{X}^{1d}(t) = \frac{1}{24\text{ hours}} \int\limits_0^{24\text{ hours}} X(t - t')dt'. \tag{17}$$

Without this correction, the simulation of diurnal cycle would be damped by nudging.

2025, **26** (3), 380–395. doi 10.26089/NumMet.v26r325

Let us consider the numerical scheme of nudging for the ocean model in details. Similarly to the atmosphere model of the INMCM5, the ocean model also uses splitting by physical processes [42]. The simplified scheme can be written as

$$\frac{\tilde{X}^n - X^n}{\Delta t} = F(X^n), \tag{18}$$

$$\frac{X^* - \tilde{X}^n}{\Delta t} = A(\tilde{X}^n), \tag{19}$$

$$\frac{X^{n+1} - \tilde{X}^n}{\Delta t} = A(X^*). \tag{20}$$

Integrating the advection-diffusion processes is done using explicit one-step Matsuno scheme with two stages given by (19) and (20).

The daily average value (17), used in ocean nudging tendency, is approximated using

$$\left(\overline{X}^{1d}\right)^n = \frac{1}{M}\sum_{k=0}^{M-1} X^{n-k}, \quad M = \frac{24 \text{ hours}}{\Delta t}.$$

This averaging leads to the fact that the numerical scheme with nudging actually has M steps.

Similarly to the atmosphere model we apply the scheme (18)–(20) to a scalar model equation $\dot{x} = i\omega x$. This results in the following difference problem:

$$\frac{\tilde{x}^n - x^n}{\Delta t} = \frac{1}{\tau_{\text{oc}}}\left(x_R - \frac{1}{M}\sum_{k=0}^{M-1} x^{n-k}\right), \tag{21}$$

$$\frac{x^* - \tilde{x}^n}{\Delta t} = i\omega\tilde{x}^n, \tag{22}$$

$$\frac{x^{n+1} - \tilde{x}^n}{\Delta t} = i\omega x^*. \tag{23}$$

The von Neumann stability analysis of the problem gives the following equations for $\xi = \delta^{n+1}/\delta^n$ and $\mu = \tilde{\delta}^n/\delta^n$:

$$\frac{\mu - 1}{\Delta t} = -\frac{1}{M\tau_{\text{oc}}}\frac{1 - \xi^{-M}}{1 - \xi^{-1}},$$
$$\xi = r(i\omega\Delta t)\mu.$$

Here $r(z) = 1 + z + z^2$ is the stability function of the Matsuno scheme. The equation for ξ is of M-th degree and can hardly be solved for ξ. Instead, let us apply the root locus curve method [46] often used to analyze stability of multistep methods. Primarily, let us solve the equation for $r(\xi)$.

$$r = \xi\left(1 - \frac{\Delta t}{M\tau_{\text{oc}}}\frac{1 - \xi^{-M}}{1 - \xi^{-1}}\right)^{-1}.$$

On the other hand, r is related to ω by $r = 1 + i\omega\Delta t - (\omega\Delta t)^2$. Knowing r, the values of ω are given by

$$\omega_{1,2} = \frac{i \pm \sqrt{3 - 4r}}{2\Delta t}. \tag{24}$$

We are interested in which values of $\omega \in \mathbb{R}$ belong to the stability region $|\xi| \leqslant 1$.

The idea of the root locus curve method is to parameterize the border of the stability region $|\xi| = 1$ using $\xi = e^{i\alpha}, \alpha \in [0, 2\pi]$. Taking into account (24), the values of $r(e^{i\alpha})$ can be mapped to a pair of ω values, resulting in a pair of parametric curves $\omega_{1,2}(\alpha)$. The curves (up to Δt scale) depend only on values of parameters M and $\gamma \equiv \dfrac{\Delta t}{\tau_{\text{oc}}}$.

Figure 1 shows that the stability region for real values ω strongly depends on γ. For small values of $\gamma \leqslant \gamma_{\text{crit}}$ the stability region is almost identical to the one of the Matsuno scheme ($|\omega\Delta t| \leqslant 1$), but for large values $\gamma > \gamma_{\text{crit}}$ the bordering curves intersect the real axis near the origin, reducing the stability region

2025, **26** (3), 380–395. doi 10.26089/NumMet.v26r325

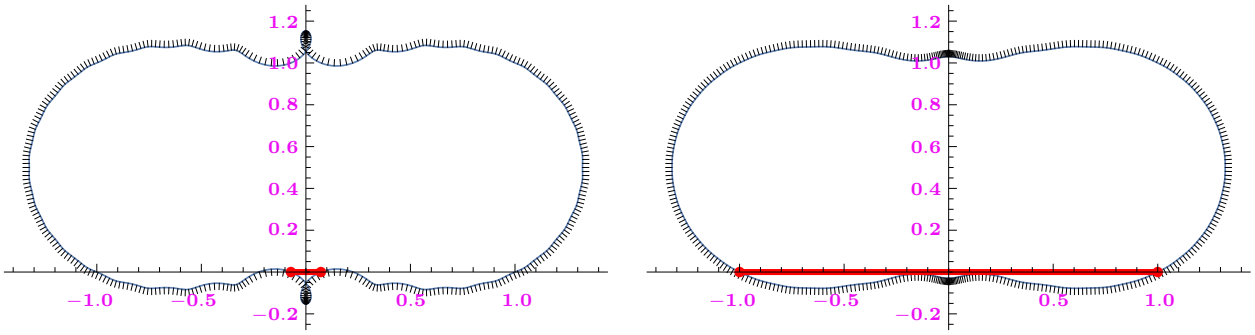

a) b)

Figure 1. Curves that enclose the stability regions on the $\omega\Delta t$ complex plane: a) $M = 20$, $\gamma = 0.15$; b) $M = 20$, $\gamma = 0.03$. Ticks along the curves indicate the exterior of the stability region. The real valued stability region for $\omega\Delta t$ is highlighted using a red segment

dramatically. The reduction becomes even more dramatic if we consider $M = 120$, which corresponds to the time step $\Delta t = 0.2$ hour in the INMCM5 ocean model.

The value γ_{crit} can be found numerically from the system describing the real axis tangency condition:

$$\begin{cases} \operatorname{Im} \omega_2(M, \gamma_{\text{crit}}, \alpha_{\text{crit}}) = 0, \\ \operatorname{Im} \dfrac{\partial \omega_2}{\partial \alpha}(M, \gamma_{\text{crit}}, \alpha_{\text{crit}}) = 0. \end{cases}$$

The critical value γ_{crit} depends on M only. For $M = 10 \div 1000$ the critical value is well approximated by $\gamma_{\text{crit}} \approx \dfrac{42}{M^2}$. For $M = 120$ we obtain $\gamma_{\text{crit}} = 5.83 \cdot 10^{-4}$ and $\tau_{\text{oc}} \geqslant 68.6$ hours $= 2.85$ days.

When γ is subcritical (τ_{oc} is not too small), the stability condition for the scheme coincides with the one of the Matsuno scheme $|\omega\Delta t| \leqslant 1$ without any nudging. In practice the scheme may be stable even for smaller τ_{oc} if more dissipative physical terms are taken into account.

The characteristic relaxation time τ_{oc} for ocean fields was chosen to be 7 days. Reducing this time to 1 day strongly affects the thermodynamics of sea ice, while increasing it to 14 days leads to noticeable errors between the simulated and reanalysis fields.

4. Climate simulations under relaxation. To investigate how climate simulation quality depends on which components of climate system are nudged to the reanalyses data, we conducted the following three experiments:

1) ATM — relaxation of 3D fields of air temperature, zonal and meridional components of velocity;
2) ATM+OC — combining ATM and relaxation of 3D fields of sea water potential temperature and salinity;
3) FA+OC — ATM+OC experiment, but without relaxation in lower 5 atmosphere levels ($\sigma \geqslant 0.85$) [47].

All relaxation experiments started on January 1, 1990 and ended on December 31, 2020. The experiments follow the CMIP6 [2] protocol: for years of 1990–2014 all external forcings are historical and for years of 2015–2020 forcings are set from SSP3-7.0 scenario [6, 7]. In all experiments $\tau_{\text{atm}} = 6$ hours, $\tau_{\text{oc}} = 1$ week.

We compare the modern climate simulations obtained in the relaxation experiments with ERA5 [23] atmospheric reanalysis, SODA3.4.2 oceanic reanalysis and CERES–EBAF [48] observations for the top of atmosphere (TOA) irradiances, and also with the ensemble of the INMCM5 experiments from CMIP6 (HIST+SSP3-7.0). This ensemble consists of 15 members of historical experiment (1991–2014) and its extension using the SSP3-7.0 scenario (2015–2020). To eliminate spin-up effects, the comparison is made for period of 1991–2020. The climate comparison is made on the INMCM5 model grid for atmospheric fields and on $0.5° \times 0.5°$ latitude-longitude grid for ocean fields.

Table 1 shows the root mean square error (RMSE) relative to ERA5 and CERES-EBAF data for general atmospheric fields for HIST+SSP3-7.0 and all relaxation experiments. We compute RMSE only for those atmospheric fields that are not directly nudged by the relaxation procedures. For near-surface air temperature, sea level pressure, total precipitation, sufrace temperature, geopotential height at 500 hPa level and longwave cloud radiative forcing, in all relaxation experiments the RMSE is significantly lower then in HIST+SSP3-7.0 ensem-

2025, **26** (3), 380–395. doi 10.26089/NumMet.v26r325

Table 1. The RMSE (averages for 1991–2020) of INMCM5 relative to the ERA5 reanalysis and the CERES-EBAF satellite data. The best value for each field is highlighted in green

Field	HIST+SSP3-7.0	ATM	ATM+OC	FA+OC
near-surface air temperature, K	1.97	1.52	1.42	1.50
sea level pressure, hPa	1.84	1.63	1.62	1.67
total precipitation, mm/day	1.33	0.93	0.92	1.04
TOA outgoing shortwave radiation, W/m^2	12.6	12.4	13.2	13.0
TOA outgoing longwave radiation, W/m^2	8.70	6.80	7.50	6.22
surface temperature, K	2.23	1.96	1.75	1.77
humidity at 850 hPa level, 10^{-3}	0.68	0.77	0.58	0.63
humidity at 200 hPa level, 10^{-5}	0.69	0.62	0.79	0.70
geopotential height at 500 hPa level, m	43.9	24.5	24.4	23.6
shortwave cloud radiative forcing, W/m^2	12.1	12.5	12.4	11.6
longwave cloud radiative forcing, W/m^2	9.10	5.82	6.12	5.71

ble. Applying relaxation in the ocean model reduces RMSE not only for near-surface and surface temperatures, but also for humidity at 850 hPa. The experiment FA+OC demonstrates the least RMSE for outgoing longwave radiation and both short- and longwave cloud radiative forcings, indicating improvements in simulation of cloudiness.

Not only the RMSE decrease is important for good quality of climate simulation, but also how the global mean model values are close to the reanalysis data. Figure 2 shows timeseries of the global mean annual near-surface air temperature for the HIST+SSP3-7.0 experiment, for different relaxation experiments and ERA5 data. The HIST+SSP3-7.0 ensemble simulates the observed trend well, but significantly underestimates the value of the near-surface temperature. At the same time, in all relaxation experiments the global mean near-surface air temperature became much closer to ERA5.

As we can see in Figure 2, the global mean annual near-surface air temperature in the ATM+OC and FA+OC experiments is closer to the ERA5 reanalysis than the one obtained in the ATM experiment. We may

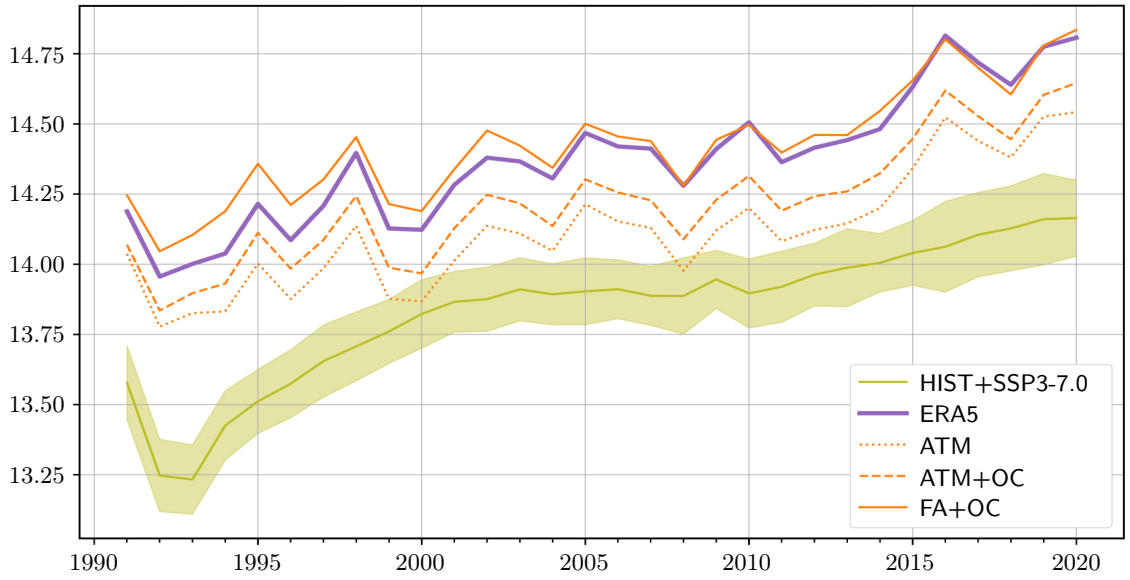

Figure 2. Timeseries of the global mean annual near-surface air temperature (°C) in 1991–2020 according to the HIST+SSP3-7.0 ensemble and the INMCM5 relaxation experiments. The olive line and olive shaded region are the mean and standard deviation from the ensemble mean for 15 calculations of the historical experiment with INMCM5. The purple line corresponds to ERA5 data. The orange lines denote the different relaxation experiments: dotted line — ATM, dashed line — ATM+OC, solid line — FA+OC

2025, **26** (3), 380–395. doi 10.26089/NumMet.v26r325

conclude that enabling relaxation in the ocean model is crucial to obtain results that are close to reanalysis. The FA+OC experiment, where no relaxation is done in the lower 5 vertical levels of the atmosphere, demonstrates the best simulation of the global mean annual near-surface air temperature, especially after 1995. In this experiment the lower atmosphere (including near-surface and boundary layers) adapts itself to the ocean surface and the free atmosphere by means of model vertical processes only. In this case the model is allowed to conform the atmosphere and ocean model physics, including evaporation, condensation and cloud formation processes, which probably leads to better simulation of the near-surface fields mean state.

Figure 3 shows the 1991–2020 climatology biases relative to SODA3.4.2 data for sea surface salinity and zonal averaged sea water potential temperature in HIST+SSP3-7.0 and two relaxation experiments.

The HIST+SSP3-7.0 experiment has the most notable error in sea surface salinity (more than 2.5 PSU) in the Arctic region and a rather large bias over the Pacific and Indian oceans. The notable bias in sea surface salinity is also observed in the Atlantic ocean, related to the incorrect Gulfstream separation due to flaws of vertical coordinate σ used in the INMCM5 ocean model. Applying relaxation only in the atmosphere model barely decreases the bias of the sea surface salinity in the east of the Arctic region, in the Northern Atlantic and in the Indian ocean, but the overall bias in the Arctic and Pacific oceans remains notable. The bias for sea surface salinity decreases significantly only when relaxation in the ocean model is turned on.

For the sea water potential temperature the HIST+SSP3-7.0 experiment shows large bias in the upper mixed ocean layer both in tropics and mid-latitudes. The greatest underestimation is observed at nearly 100 m depth in the tropics of the Pacific ocean. In the deep ocean layers the error is concentrated in high latitudes of the Northern Hemisphere. In contrast with the sea surface salinity applying relaxation only in the atmosphere model significantly reduces bias of the sea water potential temperature in the ocean upper mixed layer. The deep ocean temperature bias in the experiment with atmosphere relaxation remains the same as in HIST+SSP3-7.0.

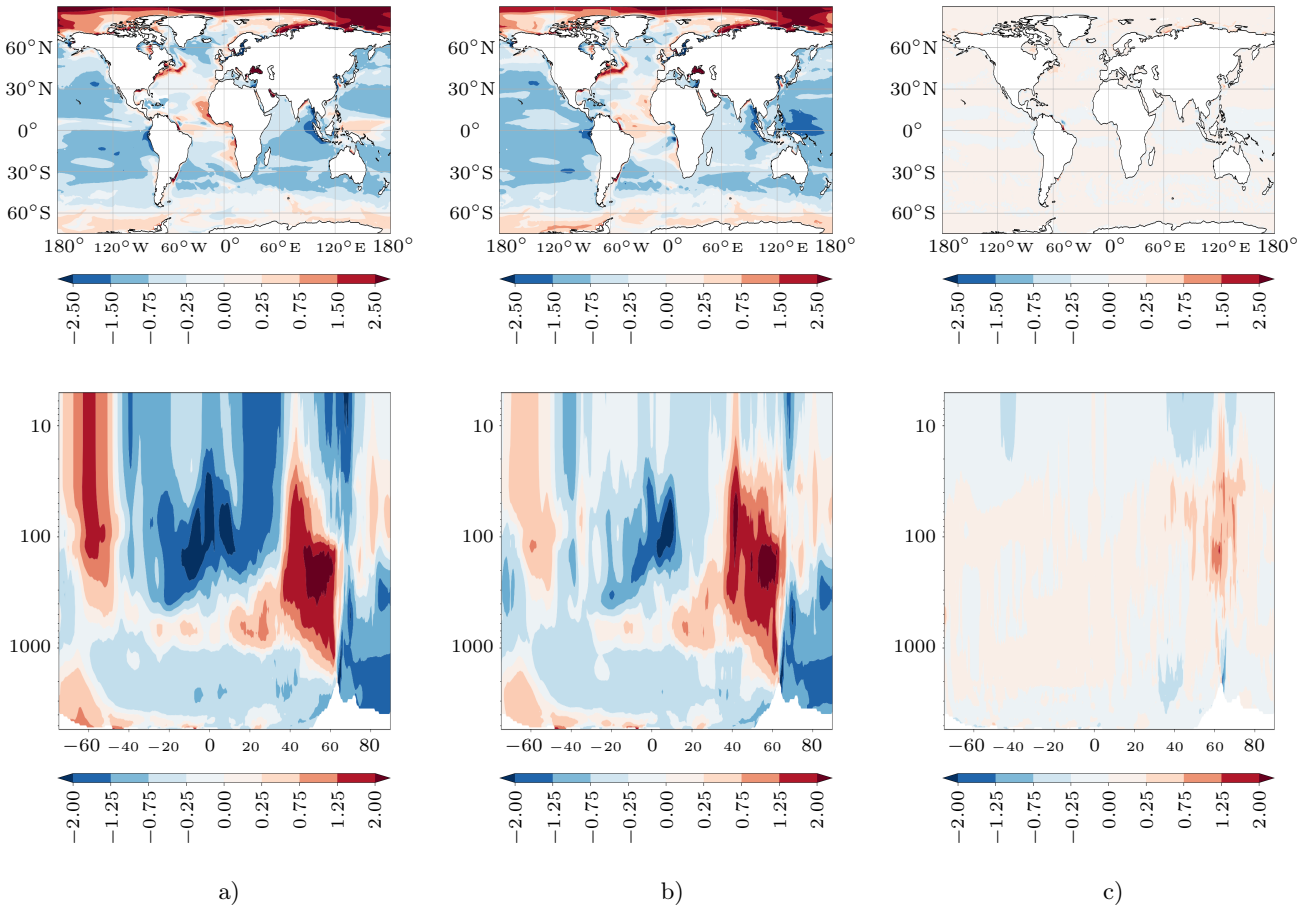

Figure 3. Biases for sea surface salinity (top row, in PSU) and sea water potential temperature (bottom row, in °C) in three experiments (1991–2020, relative to SODA3.4.2 reanalysis data): a) ensemble of HIST+SSP3-7.0 experiment; b) ATM relaxation experiment; c) ATM+OC relaxation experiment

2025, **26** (3), 380–395. doi 10.26089/NumMet.v26r325

Applying relaxation in the ocean model eliminates majority of bias in the sea water potential temperature both in the upper mixed ocean layer and in the deep ocean. Despite this, the bias over the high latitudes of the Northern Hemisphere, induced by the use of the terrain-following σ-coordinate in the INMCM5 ocean model, still remains, but its magnitude is substantially reduced.

Summing up the results presented in Table 1 and Figures 2, 3, we may conclude that application of nudging significantly improves the simulation of modern climate in comparison with HIST+SSP3-7.0. Applying relaxation in the ocean model is necessary to eliminate the INMCM5 bias in deep ocean layers. To reduce the INMCM5 errors in cloudiness, near-surface and atmosphere boundary layers it is crucial to eliminate relaxation in the lower atmosphere to avoid distortions of the simulated physical phenomena.

5. Seasonal hindcasts with INMCM5. When calculating seasonal hindcasts, the INMCM5 is basically [13] initialized in terms of anomalies (Anom): reanalyses anomalies are added to the model climatology obtained by averaging data from the CMIP6 HIST+SSP3-7.0 experiments ensemble. The anomaly initialization technique is applied to the following prognostic variables of the INMCM5:

- air temperature and humidity;
- horizontal components of wind speed;
- surface pressure and temperature;
- soil temperature and moisture;
- snow water equivalent;
- sea water potential temperature;
- sea water salinity;
- sea surface height;
- sea ice concentration and thickness.

To create the initial states, the ERA5 data is used for the atmosphere and land surface, whereas the SODA3.4.2 data is used for the ocean and sea ice.

In this study, we apply the reanalyses full field initialization (Full) to the INMCM5 seasonal hindcasts. Air temperature and humidity, horizontal components of wind speed, sea water potential temperature and sea water salinity, sea surface height, sea ice concentration and thickness are set as full fields from the ERA5 and SODA3.4.2 data. At the same time, surface pressure, surface temperature, snow water equivalent, soil temperature and moisture are still initialized in terms of anomalies to avoid shock from the initial data.

We also use the initial states saved during the climate experiments under relaxation (ATM, ATM+OC, FA+OC) to compute seasonal hindcasts. In this case the whole INMCM5 is initialized with the results of the relaxation experiments, except for the sea ice concentration and thickness that are set in the full fields of the SODA3.4.2 reanalysis.

The ensemble of the initial states is generated by introducing a smooth long-wave disturbance with an amplitude of 0.1 K into the initial state of air temperature at all model σ-levels at each point of the model grid. The ensemble consists of 20 realizations.

The INMCM5 seasonal hindcasts also follow the CMIP6 protocol: for 1990–2014 all external forcings are historical and for 2015–2020 forcings are set from SSP3-7.0 scenario.

6. Quality of November–March hindcasts from the relaxed initial states. To study the impact of different initialization methods on the quality of the INMCM5 seasonal hindcasts, we performed the following series of hindcasts for the November–March with initial states set using the anomaly initialization technique (Anom), the full field initialization (Full) and the initial states obtained from the climate experiments under relaxation (ATM, ATM+OC, FA+OC). Each series starts on November 1, 1991–2020 and lasts for 5 months.

The temporal anomaly correlation coefficients (ACC) for near-surface air temperature (T2), sea level pressure (SLP), air temperature at 850 hPa level (T850) and geopotential height at 500 hPa level (H500) are used to evaluate the quality of the different INMCM5 hindcast series. The ERA5 reanalysis data is used as observations. The ACC are calculated from the mean values for December–February 1991/1992–2020/2021 and are averaged over the following regions:

- Gl — Globe;
- NE — Northern Extratropics (20°–90°N);
- SE — Southern Extratropics (20°–90°S);
- Tr — Tropics (20°S–20°N).

2025, **26** (3), 380–395. doi 10.26089/NumMet.v26r325

We also compute the Globe averaged temporal ACC for each hindcast month from November to March. Before calculating all these scores, the INMCM5 hindcasts and the ERA5 reanalysis data are interpolated to a regular latitude–longitude 2.5° × 2.5° grid adopted by World Meteorological Organization for long-range forecasts verification [49].

Here we compare scores of hindcasts series from different relaxation initial states with the Anom and Full technique. Table 2 presents the temporal anomaly correlation coefficients of the T2, SLP, T850, H500 hindcasts for the Northern Hemisphere winter season (December–February, DJF) computed using different initialization methods.

Full field initialization shows notable improvement of ACC for all mentioned variables in all regions except the Northern Extratropics. The ATM series slightly outperforms the anomaly initialization only in tropics. When using the initial states from ATM+OC, ACC is similar to that obtained with the full field initialization and is slightly greater in the Northern Extratropics. Finally, the initialization with FA+OC initial states provides the highest ACC across all series for all variables and regions except for the Southern Extratropics. This series also shows the most notable ACC improvement in the Northern Extratropics compared to the full field initialization.

Figure 4 presents the spatial distributions of the temporal anomaly correlation coefficients for near-surface air temperature and geopotential at 500 hPa level from Anom, Full and FA+OC hindcast series. The presented spatial distributions of ACC for near-surface air temperature are very similar.

Meanwhile, a significant increase in ACC for Full and FA+OC initialization is observed over the tropics. The ACC values for FA+OC are slightly bigger than in Full over the high latitudes of the Northern Pacific Ocean and the Northern Atlantic. In contrast, the ACC distributions for H500 in Full and FA+OC series notably differ from Anom, especially in the Atlantic and Indian Ocean tropics, having better correlation in these regions. The FA+OC outperforms Full over the Atlantic Ocean, the Arctic region and the Northern Eurasia.

Let us now consider the quality of hindcasts for each single month from November to March. Figure 5 presents the globally averaged ACC for sea level pressure and air temperature at the level of 850 hPa obtained using different initialization methods. For all methods the best forecast quality of SLP and T850 is observed for the first month and generally the ACC decreases with time. For the sea level pressure the decrease is more significant than for the air temperature at 850 hPa. Compared to the full field initialization method, all hindcast series obtained using the relaxation experiments initialization demonstrate smaller ACC for November. The ATM series shows the ACC that comparable to the anomaly initialization. The ATM+OC and FA+OC series demonstrate the highest ACC in February and March among all initialization methods considered.

Table 2. The temporal anomaly correlation coefficients of the T2, SLP, T850, H500 hindcasts (DJF) over the period 1991–2020 for different regions. The best score is highlighted in green

		Anom	Full	ATM	ATM+OC	FA+OC
T2	Gl	0.47	0.51	0.46	0.51	0.51
	NE	0.38	0.38	0.31	0.40	0.42
	SE	0.37	0.43	0.39	0.41	0.40
	Tr	0.65	0.71	0.66	0.70	0.71
SLP	Gl	0.39	0.45	0.39	0.44	0.48
	NE	0.26	0.26	0.22	0.28	0.33
	SE	0.30	0.38	0.32	0.36	0.39
	Tr	0.61	0.70	0.63	0.69	0.72
T850	Gl	0.36	0.40	0.38	0.41	0.42
	NE	0.29	0.30	0.26	0.36	0.37
	SE	0.26	0.33	0.30	0.29	0.29
	Tr	0.53	0.57	0.57	0.57	0.58
H500	Gl	0.49	0.55	0.53	0.54	0.57
	NE	0.35	0.33	0.30	0.37	0.41
	SE	0.38	0.48	0.43	0.44	0.46
	Tr	0.74	0.83	0.85	0.83	0.83

2025, **26** (3), 380–395. doi 10.26089/NumMet.v26r325

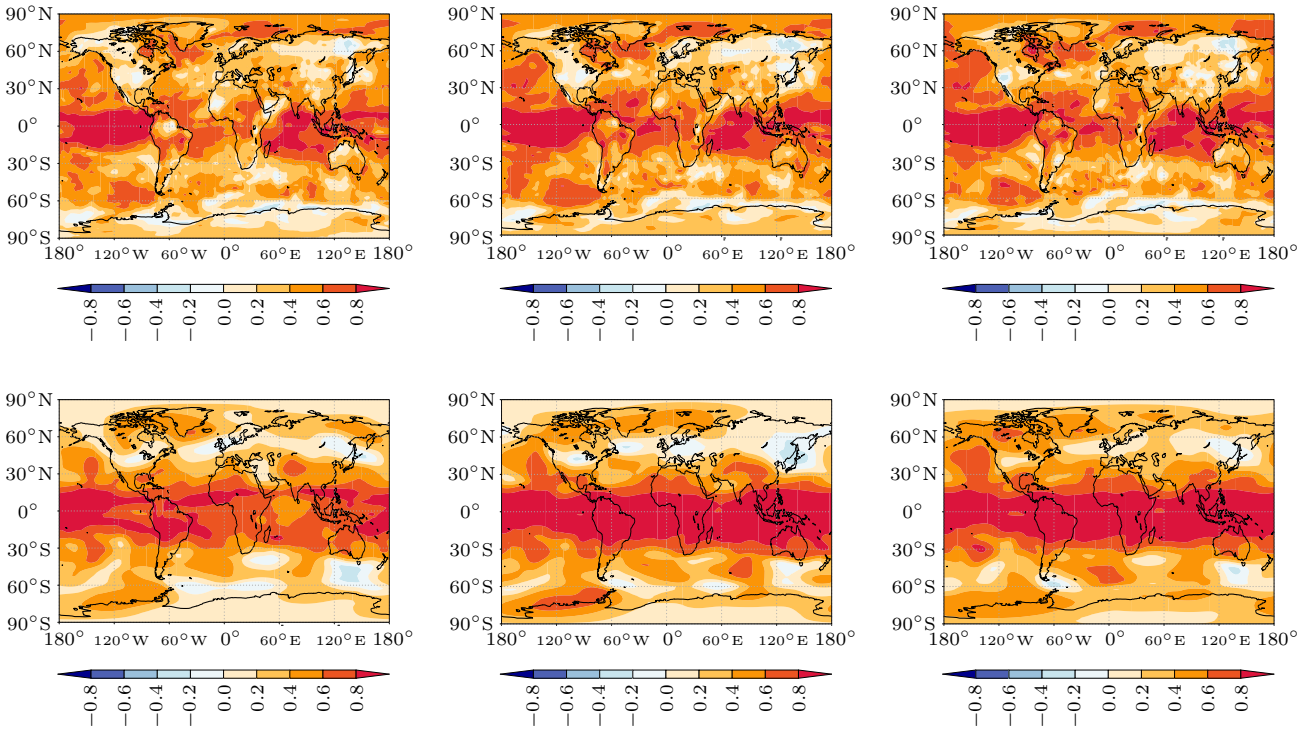

Figure 4. Spatial patterns of the temporal anomaly correlation coefficients for the DJF near-surface air temperature (top row) and the geopotential height at 500 hPa level (bottom row) in three series of hindcasts: a) Anom; b) Full; c) FA+OC

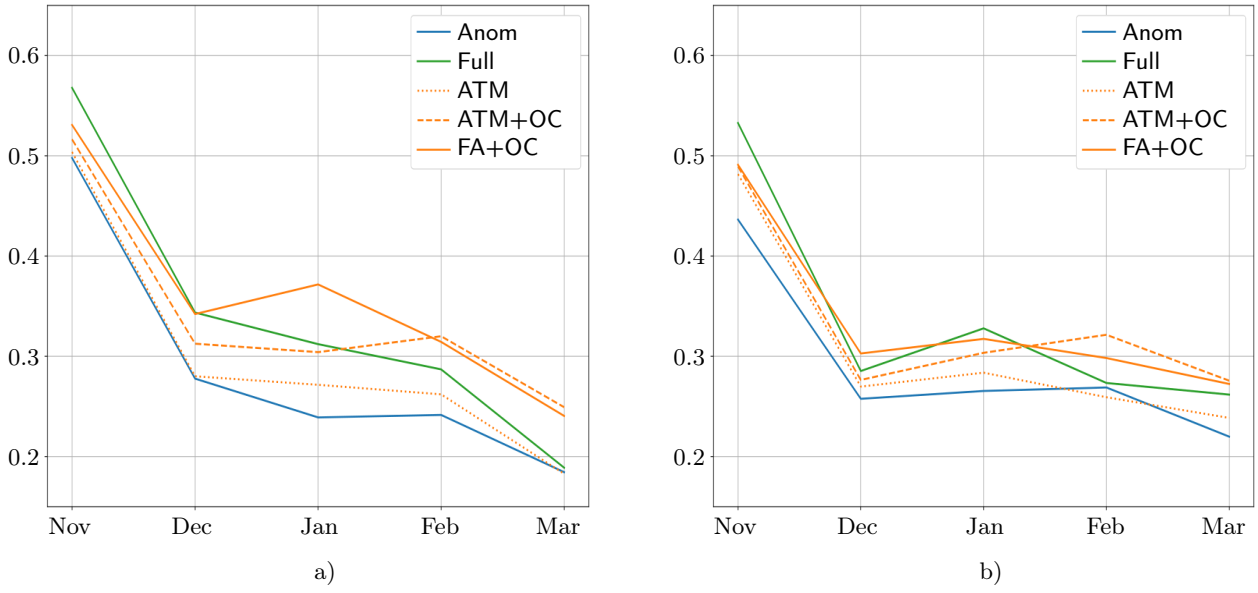

Figure 5. Globe ACC for each month of the forecast from Anom, Full and different hindcasts series from initial states obtained from relaxation experiments for: a) the sea level pressure; b) air temperature at 850 hPa level

Summing up the results obtained both for winter season hindcasts in the Northern Hemisphere with one-month lead time and for every month from November to March, we may conclude that using the initial states from relaxation experiments allows to improve results for DJF and every month, except for the first one.

2025, **26** (3), 380–395. doi 10.26089/NumMet.v26r325

7. Conclusion. In this work, we implement the nudging technique in the atmosphere and ocean models of the INMCM5 global coupled climate model. The numerical stability of the approach was validated against a model equation and the sufficient conditions for the relaxation parameter were formulated. This is the first attempt to use a simple data assimilation method for producing initial states for the INMCM5 seasonal hindcasts.

We evaluate the quality of climate simulation in different relaxation experiments to find the optimal nudging strategy and ensure that no error was introduced during implementation. Application of the nudging significantly improves the simulation of modern climate in comparison with the free INMCM5 modern climate simulation (HIST+SSP3-7.0). We also found out that using the nudging in the ocean model is necessary to eliminate the INMCM5 bias in deep ocean layers. To reduce the INMCM5 errors in cloudiness, near-surface and atmosphere boundary layers it is crucial to eliminate relaxation in the lower atmosphere to avoid distortions of the simulated physical phenomena.

We carry out several series of hindcasts for the 1991/1992–2020/2021 Northern Hemisphere winter seasons with the INMCM5 to study the influence of different initialization methods on the seasonal hindcasts quality. Results obtained using the initial states from different relaxation experiments we compare with those obtained using both reanalyses full field and anomaly initialization techniques.

For the DJF hindcasts with one-month lead time, the use of the initial states from relaxation experiments allows to increase ACC values compared to both reanalyses full field and anomaly initialization. At the same time, for the first month reanalyses full field initialization still provides the best hindcast quality. Applying nudging in the ocean model is essential to maintain hindcast skill over longer lead times than when using other initialization methods. It might be reasonable to use the initial states obtained by nudging for ultra long-range (e. g. for growing and heating seasons) and annual-to-decadal hindcasts.

References

1. E. M. Volodin, E. V. Mortikov, S. V. Kostrykin, et al., "Simulation of the present-day climate with the climate model INMCM5," Climate Dynamics **49** (11), 3715–3734 (2017). doi 10.1007/s00382-017-3539-7.
2. V. Eyring, S. Bony, G. A. Meehl, C. A. Senior, B. Stevens, R. J. Stouffer, and K. E. Taylor, "Overview of the Coupled Model Intercomparison Project Phase 6 (CMIP6) experimental design and organization," Geoscientific Model Development **9** (5), 1937–1958 (2016). doi 10.5194/gmd-9-1937-2016.
3. L. Bock, A. Lauer, M. Schlund, M. Barreiro, N. Bellouin, C. Jones, et al., "Quantifying progress across different CMIP phases with the ESMValTool," J. Geophys. Research: Atmospheres **125**, e2019JD032321 (2020). doi 10.1029/2019JD032321.
4. Y.-H. Kim, S.-K. Min, X. Zhang, J. Sillmann, and M. Sandstad, "Evaluation of the CMIP6 multi-model ensemble for climate extreme indices," Weather and Climate Extremes **29**, 100269 (2020). doi 10.1016/j.wace.2020.100269.
5. E. Volodin and A. Gritsun, "Nature of the Decrease in Global Warming at the Beginning of the 21st Century," Dokl. Earth Sc. **482** (1), 1221–1224 (2018). doi 10.1134/S1028334X18090210.
6. B. C. O'Neill, C. Tebaldi, D. P. van Vuuren, et al., "The Scenario Model Intercomparison Project (ScenarioMIP) for CMIP6," Geoscientific Model Development **9**, 3461–3482 (2016). doi 10.5194/gmd-9-3461-2016.
7. M. Meinshausen, Z. R. J. Nicholls, J. Lewis, et al., "The shared socio-economic pathway (SSP) greenhouse gas concentrations and their extensions to 2500," Geoscientific Model Development **13**, 3571–3605 (2020). doi 10.5194/gmd-13-3571-2020.
8. C. Tebaldi, K. Debeire, V. Eyring, et al., "Climate model projections from the Scenario Model Intercomparison Project (ScenarioMIP) of CMIP6," Earth Syst. Dynam. **12**, 253–293 (2021). doi 10.5194/esd-12-253-2021.
9. W. Hazeleger, C. Severijns, T. Semmler, et al., "EC-Earth: A Seamless Earth-System Prediction Approach in Action," Bulletin of the American Meteorological Society **91** (10), 1357–1364 (2010). doi 10.1175/2010BAMS2877.1.
10. B. Hoskins, "The potential for skill across the range of the seamless weather-climate prediction problem: a stimulus for our science," Q.J.R. Meteorol. Soc. **139** (672), 573–584, (2013). doi 10.1002/qj.1991.
11. M. A. Tolstykh, J.-F. Geleyn, E. M. Volodin, et al., "Development of the multiscale version of the SL-AV global atmosphere model," Russ. Meteorol. Hydrol. **40**, 374–382 (2015). doi 10.3103/S1068373915060035.
12. V. V. Vorobyeva and E. M. Volodin, "Experimental Studies of Seasonal Weather Predictability Based on the INM RAS Climate Model," Mathematical Models and Computer Simulations **13** (4), 571–578 (2021). doi 10.1134/S2070048221040232.

13. V. M. Khan, E. N. Kruglova, V. A. Tishchenko, et al., "Verification of Seasonal Ensemble Forecasts Based on the INM-CM5 Earth System Model," Russ. Meteorol. Hydrol. **49**, 587–597 (2024). doi 10.3103/S1068373924070033.
14. V. V. Vorobeva, E. M. Volodin, A. S. Gritsun, and M. A. Tarasevich, "Analysis of the Atmosphere and the Ocean Upper Layer State Predictability for up to 5 Years Ahead Using the INMCM5 Climate Model Hindcasts," Russ. Meteorol. Hydrol. **48** (7), 581–589 (2023). doi 10.3103/S106837392307004X.
15. M. A. Tarasevich and E. M. Volodin, "The Influence of Autumn Eurasian Snow Cover on the Atmospheric Dynamics Anomalies during the Next Winter in INMCM5 Model Data," Supercomput. Front. Innov. **8** (4), 24–39 (2021). doi 10.14529/jsfi210403.
16. P. N. Vargin, V. V. Bragina, E. M. Volodin, et al., "Investigation of the Predictability of the Arctic Stratospheric Polar Vortex Variability in the INMCM5 Seasonal Predictions," Russ. Meteorol. Hydrol. **49**, 700–710 (2024). doi 10.3103/S1068373924080053.
17. V. V. Bragina, M. A. Tarasevich, and E. M. Volodin, "Prediction of the Arctic Sea Ice Characteristics for Summer Seasons Using the INM RAS Earth System Model," Russ. Meteorol. Hydrol. **49**, 681–690 (2024). doi 10.3103/S106837392408003X.
18. Y. D. Resnyanskii, A. A. Zelen'ko, B. S. Strukov, et al., "Assessment of the Reproducibility of Oceanographic Fields in Retrospective Forecasts Using the INM-CM5 Earth System Model," Russ. Meteorol. Hydrol. **49**, 183–194 (2024). doi 10.3103/S1068373924030014.
19. L. Garcia-Oliva, F. Counillon, I. Bethke, and N. Keenlyside, "Intercomparison of initialization methods for seasonal-to-decadal climate predictions with the NorCPM," Clim. Dyn. **62**, 5425–5444 (2024). doi 10.1007/s00382-024-07170-w.
20. W. J. Merryfield, J. Baehr, L. Batté, et al., "Current and Emerging Developments in Subseasonal to Decadal Prediction," Bull. Amer. Meteor. Soc. **101** (6), E869–E896 (2020). doi 10.1175/BAMS-D-19-0037.1.
21. D. M. Smith, S. Cusack, A. W. Colman, et al., "Improved Surface Temperature Prediction for the Coming Decade from a Global Climate Model", Science **317**, 796–799 (2007). doi 10.1126/science.1139540.
22. A. Carrassi, R. J. T. Weber, V. Guemas, et al., "Full-field and anomaly initialization using a low-order climate model: a comparison and proposals for advanced formulations," Nonlin. Processes Geophys. **21** (2), 521–537 (2014). doi 10.5194/npg-21-521-2014.
23. H. Hersbach, B. Bell, P. Berrisford, et al., "The ERA5 global reanalysis," Q.J.R. Meteorol. Soc. **146**, 1999–2049, (2020). doi 10.1002/qj.3803.
24. J. A. Carton, G. A. Chepurin, and L. Chen, "SODA3: A New Ocean Climate Reanalysis," Journal of Climate **31** (17), 6967–6983 (2018). doi 10.1175/JCLI-D-18-0149.1.
25. J. A. Carton, S. G. Penny, and E. Kalnay, "Temperature and Salinity Variability in the SODA3, ECCO4r3, and ORAS5 Ocean Reanalyses, 1993–2015", Journal of Climate **32** (8), 2277–2293 (2019). doi 10.1175/JCLI-D-18-0605.1.
26. D. P. Mulholland, P. Laloyaux, K. Haines, et al., "Origin and Impact of Initialization Shocks in Coupled Atmosphere–Ocean Forecasts," Monthly Weather Rev. **143** (11), 4631–4644 (2015). doi 10.1175/MWR-D-15-0076.1.
27. J. E. Hoke and R. A. Anthes, "The Initialization of Numerical Models by a Dynamic-Initialization Technique," Monthly Weather Review **104** (12), 1551–1556 (1976). doi 10.1175/1520-0493(1976)104<1551:TIONMB>2.0.CO;2.
28. R. Bilbao, S. Wild, P. Ortega, et al., "Assessment of a full-field initialized decadal climate prediction system with the CMIP6 version of EC-Earth," Earth Syst. Dynam. **12** (1), 173–196 (2021). doi 10.5194/esd-12-173-2021.
29. A. Düsterhus and S. Brune, "Decadal predictability of seasonal temperature distributions," Geophysical Research Letters **51**, e2023GL107838 (2024). doi 10.1029/2023GL107838.
30. G. A. Meehl, L. Goddard, G. Boer, et al., "Decadal Climate Prediction: An Update from the Trenches," Bull. Amer. Meteor. Soc. **95** (2), 243–267 (2014). doi 10.1175/BAMS-D-12-00241.1.
31. E. Kalnay, *Atmospheric Modeling, Data Assimilation and Predictability* (Cambridge University Press, Cambridge, 2003). doi 10.1017/CBO9780511802270.
32. APEC Climate Center. https://apcc21.org/prediction/global/model?lang=en. Cited September 17, 2025.
33. M. A. Tolstykh, R. Yu. Fadeev, V. V. Shashkin, et al., "The SLAV072L96 Model for Long-range Meteorological Forecasts," Russ. Meteorol. Hydrol. **49**, 576–586 (2024). doi 10.3103/S1068373924070021.
34. W. J. Merryfield, W.-S. Lee, G. J. Boer, et al., "The Canadian Seasonal to Interannual Prediction System. Part I: Models and Initialization," Monthly Weather Rev. **141** (8), 2910–2945 (2013). doi 10.1175/MWR-D-12-00216.1.
35. S. G. Penny, et al., *Coupled Data Assimilation for Integrated Earth System Analysis and Prediction: Goals, Challenges, and Recommendations,* WMO Tech. Rep. (World Meteorological Organization, 2017). https://repository.library.noaa.gov/view/noaa/28431/. Cited September 17, 2025.

2025, **26** (3), 380–395. doi 10.26089/NumMet.v26r325

36. A. J. Charlton-Perez, L. Ferranti and R. W. Lee, "The influence of the stratospheric state on North Atlantic weather regimes," Q.J.R. Meteorol. Soc. **144**, 1140–1151 (2018). doi 10.1002/qj.3280.
37. J. Kidston, A. Scaife, S. Hardiman, et al., "Stratospheric influence on tropospheric jet streams, storm tracks and surface weather," Nature Geoscience **8**, 433–440 (2015). doi 10.1038/ngeo2424.
38. J. W. Hurrell, "Influence of variations in extratropical wintertime teleconnections on northern hemisphere temperature," Geophys. Res. Lett. **23** (6), 665–668 (1996). doi 10.1029/96GL00459.
39. L. M. Polvani, L. Sun, A. H. Butler, et al., "Distinguishing Stratospheric Sudden Warmings from ENSO as Key Drivers of Wintertime Climate Variability over the North Atlantic and Eurasia," Journal of Climate **30** (6), 1959–1969 (2017). doi 10.1175/JCLI-D-16-0277.1.
40. E. M. Volodin and S. V. Kostrykin, "The aerosol module in the INM RAS climate model," Russ. Meteorol. Hydrol. **41**, 519–528 (2016). doi 10.3103/S106837391608001X.
41. E. M. Volodin and V. N. Lykosov, "Parametrization of heat and moisture transfer in the soil-vegetation system for use in atmospheric general circulation models: 1. Formulation and simulations based on local observational data," Izvestiya, Atmospheric and Oceanic Physics **34** (4), 405–416 (1998). https://www.researchgate.net/publication/270586916_Parameterization_of_Heat_and_Moisture_Transfer_in_the_Soil-Vegetation_System_for_Use_in_Atmospheric_General_Circulation_Models_1_Formulation_and_Simulations_Based_on_Local_Observational_Data. Cited September 17, 2025.
42. K. M. Terekhov, E. M. Volodin, and A. V. Gusev, "Methods and efficiency estimation of parallel implementation of the σ-model of general ocean circulation," Russ. J. Numer. Anal. Math. Modelling **26** (2), 189–208 (2011). doi 10.1515/rjnamm.2011.011.
43. N. G. Yakovlev, "Reproduction of the large-scale state of water and sea ice in the Arctic Ocean in 1948–2002: Part I. Numerical Model," Izvestiya, Atmospheric and Oceanic Physics **45** (3), 357–371 (2009). doi 10.1134/S0001433809030098.
44. V. Ya. Galin, E. M. Volodin, and S. P. Smyshlyaev, "Atmospheric general circulation model of INM RAS with ozone dynamics," Russian Meteorology and Hydrology **5**, 7–15 (2003). https://www.scopus.com/pages/publications/2442505832?inward. Cited September 17, 2025.
45. G. Marchuk, *Numerical Methods in Weather Prediction* (Academic Press, New York–London, 1974). doi 10.1016/B978-0-12-470650-7.X5001-4.
46. E. Hairer and G. Wanner, *Solving Ordinary Differential Equations II. Stiff and Differential-Algebraic Problems*, Ed. 2 (Springer Berlin, Heidelberg, 1996). doi 10.1007/978-3-642-05221-7.
47. P. J. Telford, P. Braesicke, O. Morgenstern, and J. A. Pyle, "Technical Note: Description and assessment of a nudged version of the new dynamics Unified Model," Atmos. Chem. Phys. **8**, 1701–1712 (2008). doi 10.5194/acp-8-1701-2008.
48. N. G. Loeb, D. R. Doelling, H. Wang, et al., "Clouds and the Earth's Radiant Energy System (CERES) Energy Balanced and Filled (EBAF) Top-of-Atmosphere (TOA) Edition-4.0 Data Product," Journal of Climate **31** (2), 895–918 (2018). doi 10.1175/JCLI-D-17-0208.1.
49. WMO Manual on the Global Data-processing and Forecasting System. Volume I (Annex IV to WMO Technical Regulations). Global Aspects, WMO-No. 485, Geneva, 2023. https://library.wmo.int/idurl/4/35703. Cited September 17, 2025.

Received *June 3, 2025*

Accepted *August 28, 2025*

Published *September 23, 2025*

Information about the authors

Maria A. Tarasevich — Junior Researcher; 1) Marchuk Institute of Numerical Mathematics RAS, Gubkina ulitsa, 8, 119333, Moscow, Russia; 2) Hydrometeorological Research Center of Russian Federation, Staromonetniy pereulok, 29, 119017, Moscow, Russia.

Evgeny M. Volodin — Dr. Sci., Leading Scientist; 1) Marchuk Institute of Numerical Mathematics RAS, Gubkina ulitsa, 8, 119333, Moscow, Russia; 2) Institute of Geography RAS, Staromonetniy pereulok, 29, 119017, Moscow, Russia.